Constraining the crustal and mantle conductivity structures beneath islands by a joint inversion of multi-source magnetic transfer functions

Chaojian Chen[1], **Alexey Kuvshinov**[1,2], **Mikhail Kruglyakov**[3,4], **Rafael Rigaud**[1]

[1]Institute of Geophysics, ETH Zürich, Switzerland
[2]Institute of the Earth's crust of Siberian branch of Russian Academy of Sciences, Irkutsk, Russia
[3]Department of Physics, University of Otago, New Zealand
[4]Geoelectromagnetic Research Center, Institute of Physics of the Earth, Moscow, Russia

Key Points:

- We develop an inversion methodology to simultaneously invert magnetotelluric and geomagnetic depth sounding transfer functions
- We implemented the methodology to constrain crustal and upper mantle conductivity beneath three island geomagnetic observatories
- Recovered conductivities reveal oceanic lithosphere of different thickness beneath each island, confirming a progressive thickening with age

Corresponding author: Chaojian Chen, `chaojian.chen@erdw.ethz.ch`

Abstract

In this study we develop a tool to simultaneously invert multi-source magnetic transfer functions (TFs), including magnetotelluric (MT) tippers (with period ranging from a few minutes to 3 hours), solar quiet (Sq) global-to-local (G2L) transfer functions (TFs; with period ranging from 6 hours to 24 hours) of ionospheric origin, and magnetospheric global Q-responses (with period ranging from a few days to a few months). We further jointly invert the aforementioned multi-source TFs to constrain the local conductivity structures beneath three islands located in South Atlantic, Indian Ocean and North Pacific. The recovered conductivity profiles suggest upper mantle plumes beneath Tristan da Cunha and Oahu islands. Besides, our results indicate resistive lithosphere of different thicknesses beneath these three islands, showing a progressive thickening of oceanic lithosphere with age.

Plain Language Summary

Determining the physical properties of the Earth's interior beneath oceans is a fundamental goal of the geoscience. One key property is electrical conductivity, which is sensitive to temperature, water and melt content. One can constrain the conductivity structure beneath oceans based on the analysis of magnetic signals measured at island geomagnetic observatories and from satellites. In this study, we jointly analyzed multi-source magnetic signals to constrain the local conductivity structures beneath three islands located in South Atlantic, Indian Ocean and North Pacific. The recovered conductivity profiles suggest upper mantle plumes beneath Tristan da Cunha and Oahu islands. Besides, our results indicate resistive lithosphere of different thicknesses beneath these three islands.

1 Introduction

Electrical conductivity provides a wealth of information on the thermal and compositional state of the Earth's interior, being highly sensitive to fractions of conductive phases, such as fluids, and partial melts [cf. *Khan*, 2016; *Karato*, 2011; *Yoshino and Katsura*, 2013]. The relatively shallow electrical structures of the Earth are conventionally studied with magnetotelluric (MT) sounding technique, whereas deeper structures are probed with geomagnetic depth sounding (GDS) method. Both methods use the transfer functions (TFs) concept to analyse and interpret the data, thus implying the work

in the frequency domain. MT TFs are either impedances, relating horizontal electric to the horizontal magnetic field or/and tippers, relating vertical to the horizontal magnetic field [*Berdichevsky and Dmitriev*, 2008]. GDS TFs are more diverse [cf. *Banks*, 1969; *Olsen*, 1998; *Schmucker*, 1999a; *Püthe et al.*, 2014; *Kuvshinov et al.*, 2021] and mostly rely on magnetic field data.

In general, continents are explored by MT and GDS methods significantly better than the oceans for two obvious reasons: a) surface observations are tied to islands that are sparsely scattered; b) seafloor observations are usually logistically as well instrumentally demanding. Despite the latter challenge, more and more seafloor MT studies are conducted [cf. *Suetsugu et al.*, 2012; *Baba et al.*, 2013, 2017a; *Key et al.*, 2013; *Naif et al.*, 2013], thus stepwise filling the substantial gap in our knowledge about the Earth's electric conductivity structure in the vast oceanic regions. However, the coverage with EM observations in the oceans remains poor. In this context, the magnetic field data from island geomagnetic observatories is considered a valuable source of information about marine electric structures. Due to the very irregular distribution of the island observatories, at most, one can constrain the local one-dimensional (1-D) conductivity structures beneath each observatory and explore the lateral variability of the recovered 1-D structures.

Previously, EM induction studies at islands primarily relied on the GDS technique being applied to either magnetic signals of magnetospheric [cf. *Khan et al.*, 2011; *Munch et al.*, 2018; *Chen et al.*, 2020] or ionospheric [cf. *Simpson et al.*, 2000; *Guzavina et al.*, 2019] origin; recall that under "ionospheric" signals, we understand variations due to solar quiet (Sq) current system (with periods ranging from a few hours to one day), and under "magnetospheric" signals – variations due to ring current (with periods ranging from a few days to a few months). With TFs estimated from these data, one can obtain 1-D conductivity profiles (beneath specific locations) in depth range of $\sim 200 - 1500$ km.

Samrock and Kuvshinov [2013] demonstrated that island MT tippers (estimated from magnetic field variations with periods ranging from a few minutes to 3 hours) are sensitive to 1-D conductivity distributions beneath islands at depths $\sim 0 - 200$ km. *Morschhauser et al.* [2019] performed "quasi" 1-D inversion of MT tippers estimated from the data at two island geomagnetic observatories and found significant lateral variability of the recovered 1-D conductivity profiles. Note that the term "quasi" is used to stress the fact

that during 1-D inversions, the three-dimensional (3-D) forward modelling operator is invoked to calculate tippers which are large due to the ocean induction effect (OIE), originated from large lateral conductivity contrasts between ocean and land [*Parkinson and Jones*, 1979; *Kuvshinov et al.*, 2002].

So far, island GDS and MT TFs were analyzed/inverted separately, resulting in a reduced vertical resolution of the recovered conductivity structures outside the target depths. Therefore, it is tempting to invert them jointly to improve the resolution and diminish uncertainties in the recovered conductivity models.

We notice that the idea of joint inversion of multi-source electromagnetic (EM) TFs is not completely new. For instance, *Egbert and Booker* [1992] and *Bahr et al.* [1993] inverted GDS TFs (in the form of conventional C-responses; [*Banks*, 1969; *Olsen*, 1998]), and MT impedances to constrain 1-D conductivity models beneath two continental sites in North America and Europe, respectively. *Grayver et al.* [2017] and *Kuvshinov et al.* [2021] obtained a globally averaged 1-D oceanic conductivity structure based on a joint analysis of satellite-detected tidal signals (in the form of tidally-induced radial magnetic field component at satellite altitude) and the signals of magnetospheric origin (in the form of global C/Q-responses). *Munch et al.* [2020] jointly inverted new GDS global-to-local (G2L) TFs [*Püthe et al.*, 2015], of both ionospheric and magnetospheric origins (to be called henceforth as Sq and Dst G2L TFs, respectively). They estimated the G2L TFs at several continental observatories and performed their 1-D inversions to detect lateral variability in the recovered 1-D conductivity profiles.

In this study, we develop a methodology to jointly invert island GDS and MT TFs for local 1-D conductivity distributions in the presence of known laterally-variable bathymetry, which controls the strength and spatial structure of OIE. Note that our previous numerical studies suggest that the proper account for the OIE requires 3-D forward modellings at fine grids, which we perform using nested domains formalism [*Chen et al.*, 2020, 2021].

We implemented the developed methodology to invert GDS and MT TFs estimated at three island geomagnetic observatories. We have chosen islands to locate in different tectonic environments, specifically, in the Indian Ocean (Cocos (West) island), in South Atlantic (Tristan da Cunha island), and North Pacific (Oahu island). We point out that since we work with island geomagnetic observatory data, the only MT TFs we can estimate are tippers. As for GDS TFs, we exploit new Sq G2L TFs [*Guzavina et al.*, 2019],

which allow us to account for the complex spatiotemporal structure of the Sq current system. We omitted longer-period, Dst G2L TFs since they appeared to be of questionable quality (non-smooth behaviour, significant uncertainties) at considered islands; recall that estimating Dst TFs requires a very long time series of observations with accurate control of the baseline, which is often not the case when one deals with island data. Due to the period range of the considered TFs – from a few minutes to one day – we constrain conductivity structures in the depth range from the surface down to approximately mantle transition zone ($\sim$ 500 km). To avoid ambiguity in conductivity distribution at larger depths, we also include into the joint inversion longer-period global Q-responses estimated by *Kuvshinov et al.* [2021].

Finally, we interpret the recovered local 1-D conductivity profiles in terms of lithosphere thickness and the presence/absence of mantle plume beneath the considered islands.

2 Methods

2.1 Magnetotelluric tippers

The source of geomagnetic field variations with periods shorter than 3 hours can be approximated by a vertically incident plane wave. This allows to relate the vertical magnetic field component, Z, with the horizontal magnetic field, $\mathbf{H}_\tau = (H_x\, H_y)$, via the tipper $T = (T_{xy}\, T_{zy})$ [*Berdichevsky and Dmitriev*, 2008]

$$Z(\mathbf{r}_s, \omega) = T_{zx}(\mathbf{r}_s, \omega) H_x(\mathbf{r}_s, \omega) + T_{zy}(\mathbf{r}_s, \omega) H_y(\mathbf{r}_s, \omega) \tag{1}$$

where $\mathbf{r}_s$ is an observation site, and $\omega = 2\pi/T$ is the angular frequency, and T is the period. Tippers were estimated in period range 5 min - 3 hours. Details on the island data to estimate tippers, and their estimation are discussed in the paper of *Rigaud et al.* [2021], seeing their section "Estimating tippers from the data". Circles with error bars in Figure 3 depict the estimated tippers.

2.2 Sq global-to-local transfer functions

The source of daily Sq variations is the ionospheric current system, which has a complex spatio-temporal structure [*Yamazaki et al.*, 2016; *Finlay et al.*, 2017]. Despite this, there were several studies that analyzed Sq variations and utilized a variant of local C-

response concept, which represents the source via a single spherical harmonic (SH) which is specific for each Sq period [cf. *Schmucker*, 1970; *Simpson et al.*, 2000; *Bahr and Filloux*, 1989]. However, presently there exists a consensus that the description of the ionospheric source by a single SH is too simplistic. Alternatively, local C-responses can be estimated without prior assumptions about the source geometry [cf. *Olsen*, 1998]. The prerequisite for the successful implementation of this approach is a relatively dense regional grid of observations in the region of interest, which is not the case with island observations.

To account for the complex spatio-temporal structure of the Sq source, we resort to (non-conventional) global-to-local transfer functions, T_n^m, that relates a set of SH expansion coefficients describing the source to a locally measured vertical magnetic field component [*Püthe et al.*, 2015; *Guzavina et al.*, 2019]

$$Z(\mathbf{r}_s, \omega) = \sum_{n,m \in L(\omega)} \epsilon_n^m(\omega) T_n^m(\mathbf{r}_s, \omega), \tag{2}$$

where $L(\omega)$ specifies a subset of SH for each Sq period ($T_p = 24/p$ hours, $p = 1, 2, 3, 4$). For details on the estimation and fundaments underlying the Sq G2L TFs, the reader is referred to the paper of *Guzavina et al.* [2019] (see their Sections 2–4). In short, for each period T_p, we determine the external (inducing) SH coefficients, ϵ_n^m, describing the source from horizontal magnetic field components measured at global net of observatories assuming a prior 3-D conductivity Earth. Then, the corresponding T_n^m are estimated by relating the local (island) vertical magnetic field component with the determined source coefficients. Only data from geomagnetic quiet days (with 48-hr average aa index smaller than 7 nT) and from equinoctial months available from 1997 until 2021 were used for Sq G2L TFs estimation. We estimated Sq G2L TFs using magnetic data measured at Cocos-Keeling Islands (CKI), Honolulu (HON) and Tristan da Cunha (TDC) geomagnetic observatories during 128, 370 and 139 magnetically quiet days, respectively. As terms with $n = p + 1$ and $m = p$ are expected to be dominant [*Schmucker*, 1999b], we analyze T_{p+1}^p only. Circles with error bars in Figure 4 represent the estimated Sq G2L TFs. It is also important to stress that the Sq data were corrected for ocean tidal signals [*Guzavina et al.*, 2018].

2.3 Global Q-responses

The source of geomagnetic field variations with periods longer than one day is primarily the magnetospheric ring current. At the Earth's surface, this source is well approximated by the $n = 1$ and $m = 0$ term, and this fact allows us to estimate global Q-responses relating the induced and inducing SH coefficients, ϵ_1^0 and ι_1^0

$$\iota_1^0(\omega) = Q_{11}^{00}(\omega)\epsilon_1^0(\omega). \tag{3}$$

Details on the data to estimate global Q-responses and on their estimation can be found in the paper of *Kuvshinov et al.* [2021], seeing their section "Estimating dominant Q-response". Circles with error bars in Figure 5 depict the estimated global Q-responses.

2.4 Forward modeling

In this study, we aim to reveal 1-D conductivity structures beneath islands. As we already discussed in Introduction, island EM TFs are substantially distorted by the ocean induction effect (OIE). To account for the OIE, we exploit a conductivity model which includes nonuniform oceanic layer(s) and 1-D mantle underneath (cf. Figure 1). Calculation of electric and magnetic fields, $\mathbf{E}$ and $\mathbf{H}$, in models with 3-D conductivity distribution, σ, requires numerically solving Maxwell's equations

$$\begin{aligned} \nabla \times \mathbf{H}(\mathbf{r}) &= \sigma(\mathbf{r})\mathbf{E}(\mathbf{r}) + \mathbf{j}^{ext}(\mathbf{r}), \\ \nabla \times \mathbf{E}(\mathbf{r}) &= i\omega\mu_0\mathbf{H}(\mathbf{r}), \end{aligned} \tag{4}$$

where $i = \sqrt{-1}$, μ_0 is the magnetic permeability of the free space, and $\mathbf{j}^{ext}$ is the extraneous current. $\mathbf{r} = (r, \theta, \phi)$ and $\mathbf{r} = (x, y, z)$ for global and Cartesian problem setups, respectively.

Our previous studies [*Chen et al.*, 2020, 2021] show that the OIE in island EM responses can be accurately accounted for by using a nested integral equation (IE) approach and invoking high-resolution bathymetry. Within the nested domain approach, the modeling is first performed at a large domain and on a coarse grid. Then the results are refined in the region of interest by performing modeling at a smaller domain and on a denser grid. In this study, we adopt the "nested" Cartesian-to-Cartesian tool [*Chen et al.*, 2021] to compute tippers and the "nested" global-to-Cartesian tool [*Chen et al.*, 2020] to compute Sq G2L TFs. In both tools, the core modules of Cartesian solver PGIEM2G [*Kruglyakov and Kuvshinov*, 2018] are used. As for the calculation of global Q-responses, we exploit

conventional IE solver by *Kuvshinov* [2008]. Different TFs – depending on their periods and spatial scale of the source – may require different discretization of the corresponding 3-D models. Specifically, for tippers calculation, we first performed modeling at a large domain and coarse lateral grid (with 180×180 cells of 2×2 km^2 size), and then at a smaller domain and finer lateral grid (with 60×60 cells of 1×1 km^2 size). As for vertical discretization, for both simulations, the 3-D modeling domain was discretized by six layers of $0.5, 0.5, 1, 1, 1.5$ and 1.5 km thicknesses. Note that since we exploit IE-based solvers, the vertical extent of the modeling domain goes down to 6 km – the maximum depth column around considered islands. To calculate Sq G2L TFs we first performed modeling at a global (spherical) grid with lateral resolution of $1^\circ \times 1^\circ$, and then at smaller (Cartesian) domain and finer lateral grid with 80×80 cells of 10×10 km^2 size, corresponding to $\sim 0.09^\circ \times 0.09^\circ$ resolution . Finally, global Q-responses are calculated at a global grid with a lateral resolution of $1^\circ \times 1^\circ$. A thin shell set-up was invoked to calculate both Sq G2L TFs and global Q-responses, meaning that the 6-km layer is substituted by a thin shell of laterally-variable conductance where the conductance is obtained as a product of bathymetry and globally averaged sea-water conductivity (3.2 S/m). Note that we performed systematic model studies to justify the parameters describing the models, namely, cell, grid and domain sizes. 3-D conductivity (or 2-D conductance) distributions in the considered models are constructed by using the $30'' \times 30''$ bathymetry data from the General Bathymetry Chart of the Oceans (GEBCO; *Becker et al.* [2009]).

2.5 Joint quasi 1-D inversion

The inverse problem is treated as an optimization problem such that

$$\phi_d(\mathbf{m}) + \lambda \phi_m(\mathbf{m}) \underset{\mathbf{m}}{\longrightarrow} \min, \tag{5}$$

where $\phi_d(\mathbf{m})$ is the data misfit, λ and $\phi_m(\mathbf{m})$ are the regularization parameter and regularization term, respectively. $\mathbf{m} = [\beta(\sigma_1), \beta(\sigma_2), \cdots, \beta(\sigma_N)]$ denotes the vector of model parameters, where $\beta(\cdot)$ is a log-based transformation ensuring the positivity of the arguments, and N is the number of parameters.

The data misfit term $\phi_d(\mathbf{m})$ reads

$$\phi_d(\mathbf{m}) = \sum_{k \in \chi} \left(\frac{1}{N_k} \sum_{i=1}^{N_k} \left| w_i^k (f_i^k(\mathbf{m}) - d_i^k) \right|^2 \right), \tag{6}$$

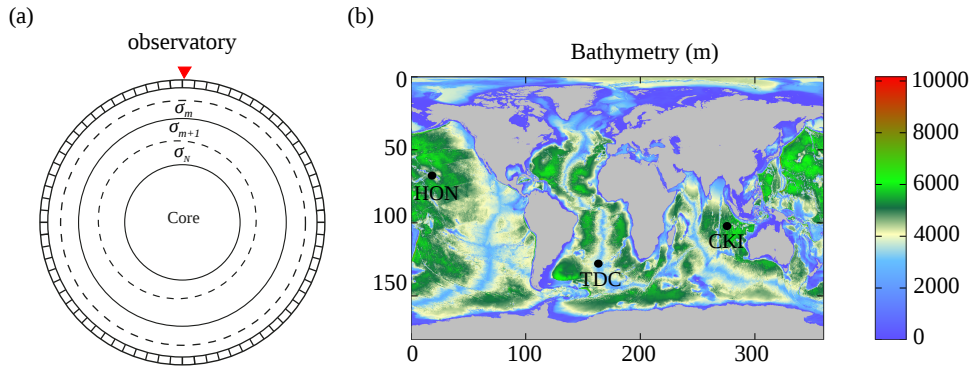

Figure 1. Left: model parameterization adopted in this study. The conductivity models consist of a 1-D layered Earth overlaid by a surface layer (or several layers) representing nonuniform conductivity distributions in the oceans and landmasses. Conductivity distributions in the surface layers(s) are constructed using bathymetry data (right); by black dots are shown locations of island geomagnetic observatories data from which are used in this paper.

where χ is a set of TFs from different methods, and w^k, f^k and d^k are the corresponding data weights, 3-D forward operator and observed (i.e. estimated from the data) TFs, respectively. Normalizing with the numbers of actual entries (N_k) aims to equate the contribution from each method in joint inversion [*Key*, 2016].

The regularization term $\phi_m(\mathbf{m})$ reads

$$\phi_m(\mathbf{m}) = \frac{1}{p_m} \sum_{j=1}^{N} |\mathbf{l}_j \mathbf{m}|^{p_m} , \tag{7}$$

where $\mathbf{l}_j$ is the regularization operator of the j-th model parameter. In our implementation, it is the first derivative with respect to the model parameters. The scalar p_m is set to 1.5, which provides a balance between sharp conductivity contrast and smooth models [*Grayver and Kuvshinov*, 2016]. The trade-off between data fit and regularization terms in the course of inversion is determined by means of the L-curve analysis [*Hansen*, 1992].

We solve the optimization problem (5) using a stochastic algorithm, called Covariance Matrix Adaptation Evolution Strategy (CMAES) method [*Hansen and Ostermeier*, 2001]. It is relevant to note here that CMAES is a global optimization method, and it finds a global minimum for a moderate number of iterations.

3 Results

We use the methodology presented in the previous section to simultaneously invert tippers, Sq G2L TFs and global Q-responses to obtain the local 1-D conductivity profiles beneath three island geomagnetic observatories (cf. their locations in Figure 1).

In the course of inversion, the 1-D part of the model is parameterized by 45 layers with thicknesses ranging from 500 meters near the surface to 200 km at the core-mantle boundary (CMB). Below CMB the conductivity is fixed to a high conductivity value – 10^5 S/m. Note that topography is not included in the model, as it has a negligible effect on the TFs in the considered period range. The starting model was taken as a homogeneous 0.01 S/m conductor down to CMB.

Figure 2 shows the recovered 1-D conductivity profiles beneath TDC, HON and CKI – coloured by red, black and blue, respectively – along with the corresponding 95% confidence intervals. The details on the recovered layered models – namely, the depths to the top of the layers, thicknesses of the layers, conductivities and their upper and lower bounds in the layers – are given in the Supporting Information. The figure also demonstrates – coloured by green – 1-D section (and corresponding confidence interval) from *Kuvshinov et al.* [2021]. This model was obtained by a joint inversion of satellite-detected radial magnetic field component due to M2 oceanic tide and global Q-responses; the model is believed to represent the globally averaged 1-D mantle structure beneath oceans.

One can see from the figure that 1-D profiles beneath each observatory differ from the globally averaged oceanic 1-D conductivity structure in the depth range from the surface down to ~ 500 km. The difference is especially noticeable in the first 100 km, i.e. at the lithospheric depths. Here the global profile appears to be much less conductive than the local profiles, thus better resolving the expected high resistance ($\sim 10^8 - 10^9$ $\Omega \cdot$ m^2) of the rigid lithosphere. The reason for the lower (less plausible) values of conductivities in the local profiles at lithospheric depths is as follows. Local profiles are obtained from the inversion of TFs, which are estimated from the magnetic field variations of ionospheric and magnetospheric origin. Due to the purely inductive excitation mechanism of these variations, and because the magnetic field on the surface of the Earth is purely poloidal, the corresponding TFs are weakly sensitive to the resistive structures in the subsurface [*Fainberg et al.*, 1990]. In contrast to these TFs, tidal magnetic fields used to constrain global oceanic conductivity at lithospheric depths are excited by motionally-

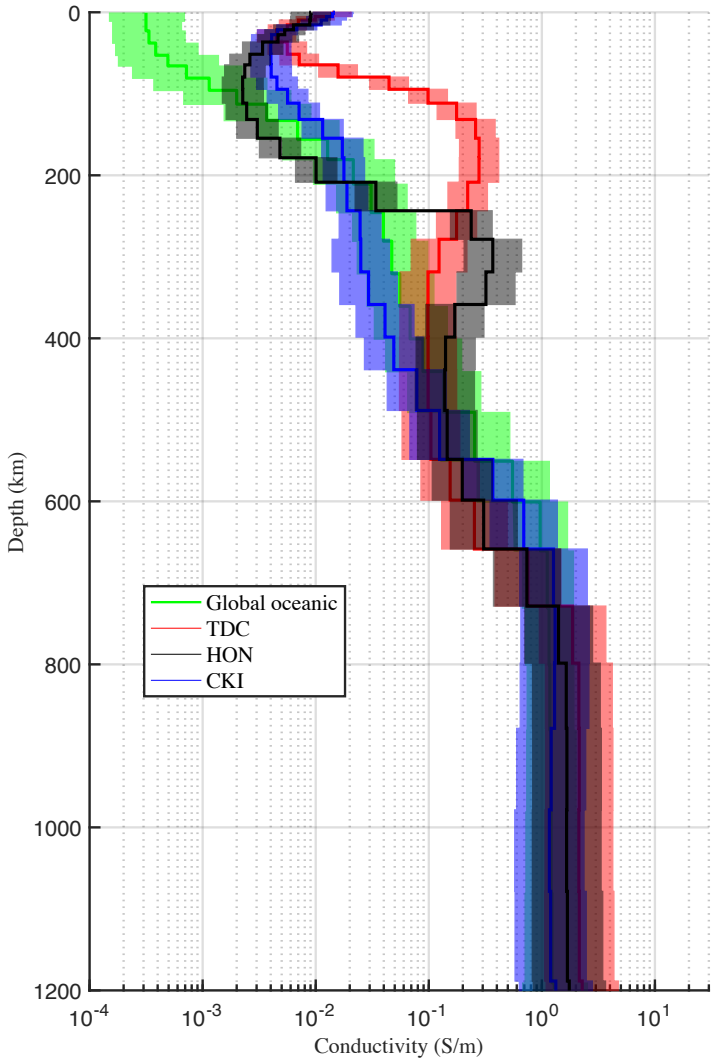

Figure 2. Recovered 1-D conductivity models along with 95 % confidence intervals beneath TDC, HON and CKI observatories by jointly inverting MT tippers, Sq G2L TFs and global Q-responses. 1-D section (and corresponding confidence interval) in green is from *Kuvshinov et al.* [2021]. The latter model was obtained by a joint inversion of satellite-detected tidal signals and global Q-response and it is believed to represent the globally averaged 1-D mantle structure beneath oceans.

driven ocean electric currents that have a unique characteristic – galvanic coupling of these currents with the Earth's subsurface. This enhances the sensitivity of the analysed magnetic fields to the Earth's resistive structures since these fields (even observed above the Earth and hence being purely poloidal) are influenced by the toroidal (galvanic) part of the primary tidal EM field. Despite less reliable values of conductivity in the local profiles at the lithospheric depths, one can interpret the results in terms of the lithosphere thickness: we will discuss this topic in Section 3.2.

As for lateral variability of the local profiles, they are – in the same (0 – 500 km) depth range – also markedly different from each other. Note that the sameness of the profiles below 500 km depth is not surprising since we used global – thus laterally-uniform – Q-responses to constrain conductivity in the lower mantle. Beneath Oahu and Tristan da Cunha islands, where mantle plumes are hypothesized [*Rychert et al.*, 2013; *Schlömer et al.*, 2017], we observe an apparent feature – an enhanced conductivity zone in the recovered profiles. However, the depth to the high-conducting zone is noticeably different in HON and TDC profiles. Beneath Tristan da Cunha island, this zone is centred at a depth of $\sim$ 180 km, which agrees with a depth where the velocity of the conduit/plume is revealed by a finite-frequency tomography [*Schlömer et al.*, 2017, cf. their Figure 9] is minimal; recall that the researchers usually associate the lower velocity zones with higher conductivity regions. The high-conducting zone beneath HON is revealed, however, at a larger depth (of $\sim$ 300 km) which is also in accordance with seismic results in that region [*Wolfe et al.*, 2009, cf. their Figure 2].

Figures 3-5 present experimental (i.e. estimated from the data) TFs and TFs computed in the local 3-D models with the recovered 1-D mantle profiles. One can observe good general agreement between the modelled and experimental TFs. The remaining (rather small, however) discrepancy could be attributed to the hypothetical 3-D conductivity structures beneath islands, which are incompatible with an assumption we made, namely, that underlying crust and mantle are 1-D. Another cause of the difference could be a potential inaccuracy of the bathymetry data.

In the next section we compare our results with the results of independent EM studies.

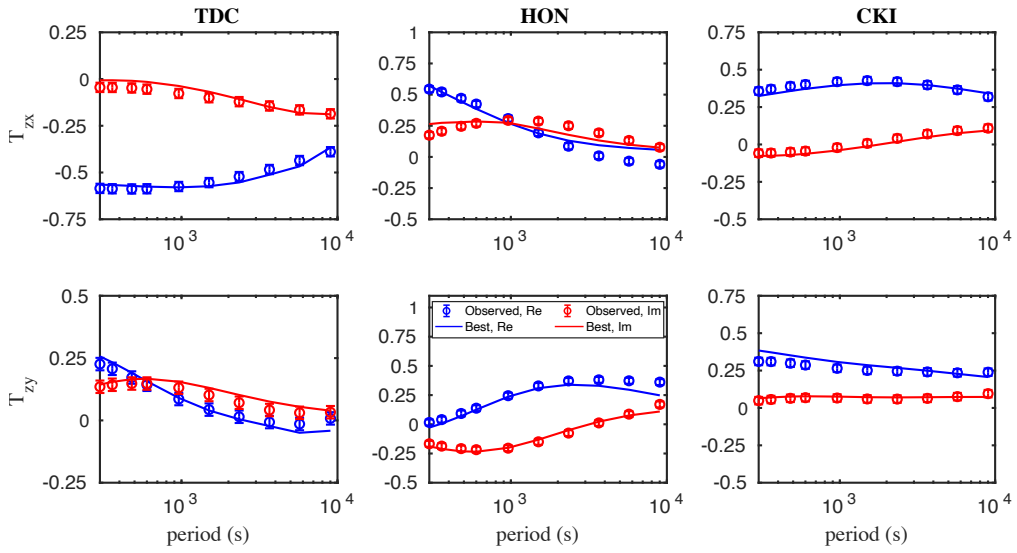

Figure 3. Comparison of the observed and modeled best-fitting MT tippers at TDC, HON and CKI observatories, respectively. Uncertainties of the observed MT tippers are indicated by the error bars.

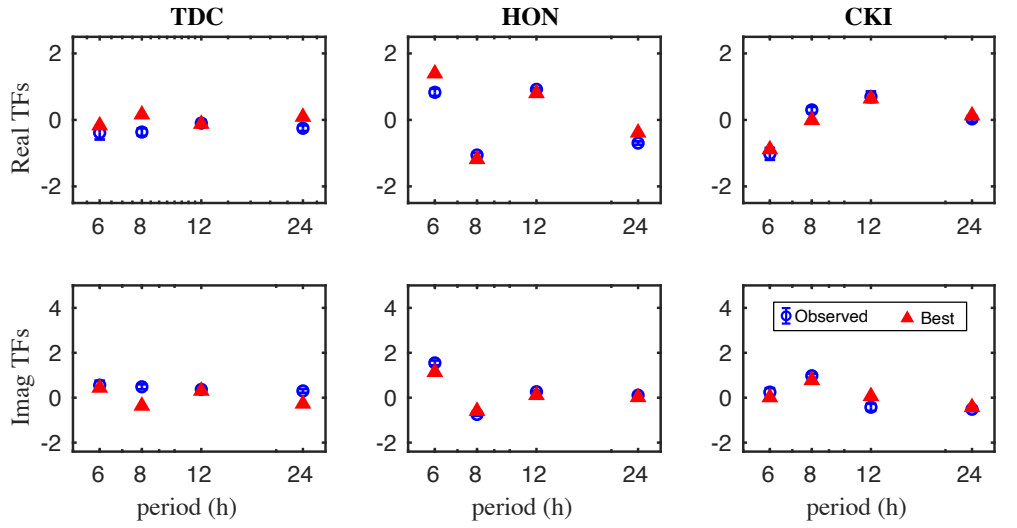

Figure 4. As in Figure 3, but for Sq global-to-local transfer functions at three island geomagnetic observatories.

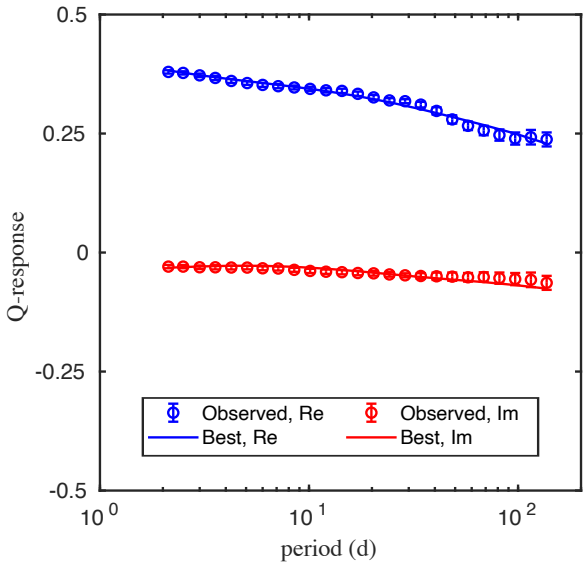

Figure 5. Comparison of the observed and modeled best-fitting global Q-responses. Uncertainties of the observed global Q-responses are indicated by the error bars.

3.1 Comparison of new 1-D profiles with the models from the independent EM studies

Figure 6a compares our 1-D profile (red) with the profiles obtained by *Morschhauser et al.* [2019] (black) and *Baba et al.* [2017a] (blue) below TDC observatory. For the reference, a globally averaged 1-D mantle structure beneath oceans from [*Kuvshinov et al.*, 2021] (green) is shown. The 1-D model of *Morschhauser et al.* [2019] was obtained by inverting the same MT tippers, using the same, quasi 1-D, problem setup and the same, CMAES, inversion technique. The distinct difference between our approaches is that we invert – along with tippers – the longer-period TFs, thus covering the wide period range between 5 minutes and 110 days; this allows us to constrain conductivity at larger depths. Bearing this information in mind, we expected to see similar conductivity distributions from the surface down to a depth of $\sim$ 100 km – which is indeed the case. Note that tippers are TFs with periods shorter than 3 hours; thus, inversion of only tippers, as it is done by *Morschhauser et al.* [2019], does not permit constraining conductivity structures at upper mantle depths reliably. This is why the profile from *Morschhauser et al.* [2019] below 100 km does not show any conductivity variations. Very low conductivities seen in a global profile at shallower depths are not reproduced in both our and *Morschhauser*

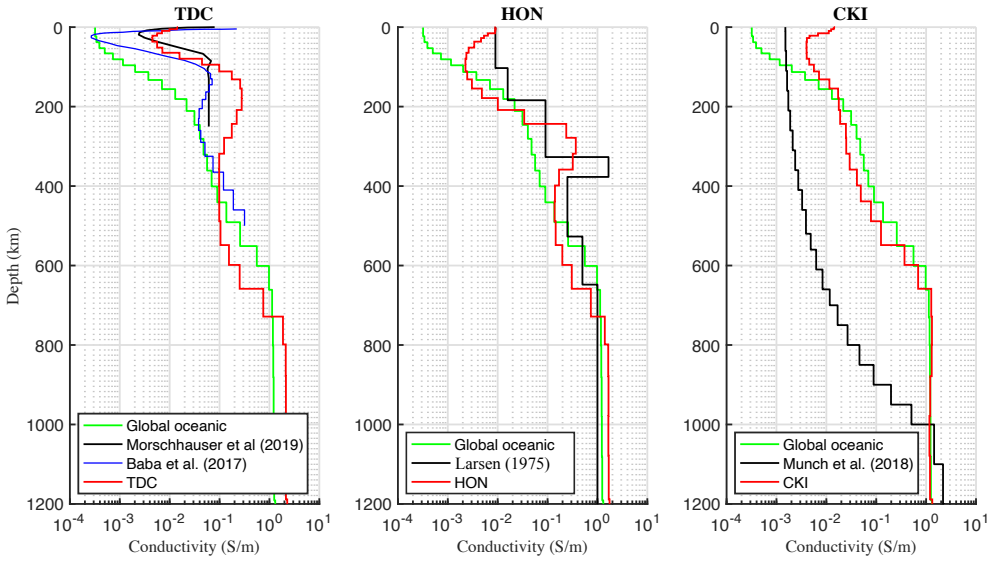

Figure 6. Comparison of the revealed 1-D conductivity profiles beneath three island observatories. Plots (a), (b) and (c) present the results for TDC, HON and CKI observatories, respectively.

et al. [2019] results. The reason for this disagreement we explained in the previous section. As for the profile from *Baba et al.* [2017a] it is much closer to a global model at depths smaller than 100 km, in terms of very low values of conductivity. We see the following explanation for that. The profile by *Baba et al.* [2017a] is obtained by an inversion of sea-bottom impedances estimated in the period range between 500 sec and two days. In contrast to our TFs estimated from the surface (purely poloidal) magnetic field, impedances are evaluated from the plane-wave horizontal electric and magnetic fields. Plane-wave horizontal electric field (in the non-1-D environment, and either at the surface or sea bottom) contains the toroidal/galvanic part, which is sensitive to the resistive lithospheric structures [*Fainberg et al.*, 1990]. Moreover, in a non-1-D environment, the sea-bottom horizontal magnetic field also comprises the toroidal constituent. This, in particular, means that the sea-bottom impedances – along with tidal signals – allow researchers to probe high-resistive/low-conducting lithosphere. Besides, their sea-bottom impedances were estimated at as long as one day; this allowed the authors to likely constrain conductivity distribution down to a depth of $\sim$ 500 km. Interestingly, their profile also contains the enhanced conductivity structure, however, less pronounced and at a slightly shallower depth.

Figure 6b compares our HON 1-D profile with that from *Larsen* [1975]. His profile was obtained by inversion of long-period (periods between 4 hours and 10 days) impedances estimated from around two years of HON observatory magnetic data and electric field measurements nearby. As the author stated, there appears to be a unquestionably resolved highly conducting zone in the depth range 330 – 380 km. Remarkably, we also reveal the enhanced conductivity zone at comparable depths. Since the minimum period in his analysis was 4 hours, it precludes resolving the structures at the shallow, 0 – 200 km, depths; this explains the difference between our and Larsen's results at these depths.

Figure 6c compares our CKI 1-D profile with that from *Munch et al.* [2018]; note that their profile is the only EM result we found in the literature for this region. As in figures for TDC and HON, globally averaged 1-D mantle structure beneath oceans [*Kuvshinov et al.*, 2021] is also shown. One can observe that starting from $\sim$ 150 km depth, our 1-D model closely follows the global profile. In particular, and in contrast to TDC and HON models, the CKI profile does not contain a high-conducting zone in the upper mantle, which agrees with an absence of plume below Cocos Islands. One can also see that profile of *Munch et al.* [2018] differs much from our and global profiles, at least, down to a depth of 1000 km. This is not completely strange, since long-period (periods longer than one day) local C-responses inverted by *Munch et al.* [2018] are only sensitive to lower mantle structures of the Earth; moreover, the lateral grid ($1^\circ \times 1^\circ$) used in their study to account for the OIE during their quasi 1-D inversion seems too coarse to reproduce OIE adequately (see *Chen et al.* [2020] for more details on this issue).

3.2 Estimating thickness of the oceanic lithosphere

The lithosphere is the rigid outermost layer of the Earth, and it is the fundamental mechanical unit of the plate tectonics theory [*Turcotte and Schubert*, 2002]. The lithosphere base, which is called a lithosphere-asthenosphere boundary (LAB), divides the rigid lid from the weaker mantle. A variety of physical parameters (seismic velocity, density and electrical conductivity) are adopted to map the thickness of the lithosphere (or depth to LAB) [*McAdoo and Sandwell*, 1985; *Winterbourne et al.*, 2009; *Rychert and Shearer*, 2009, 2011; *Grayver et al.*, 2016, among others].

Table 1. Thickness of the oceanic lithosphere, T_l, beneath TDC, HON and CKI as estimated in this study and independent studies.

Island	From where estimates of T_l are taken	T_l (km)
TDC	This study	36
	Morschhauser et al. [2019]	30
	Baba et al. [2017b]	35
	Based on eq. (8)	58
HON	This study	110
	Woods et al. [1991] and *Woods and Okal* [1996]	100
	Based on eq. (8)	127
CKI	This study	80
	Based on eq. (8)	100

We estimated the thickness of the oceanic lithosphere, T_l, beneath TDC, HON and CKI observatories from the recovered local 1-D conductivity profiles as the depth (in the shallow part of the upper mantle) from where conductivity starts to increase, after a gradual decrease at smaller depths. The same procedure was applied to estimate T_l from the conductivity profiles below TDC obtained by *Morschhauser et al.* [2019] and *Baba et al.* [2017b]. We summarize the results in Table 1. Remarkably, the estimates appeared to be rather similar, giving a thin lithosphere of ~ 36 km. As for HON, we obtain the relatively thick lithosphere with $T_l \sim 110$ km below this region. Interestingly, this value is close to an estimate of $T_l \sim 100$ km obtained by *Woods and Okal* [1996] from the seismic data in the region. Finally for CKI, we estimate T_l as ~ 80 km. Our results indicate that T_l significantly varies from island to island, but surprisingly enough that by averaging local estimates, we get a value, 75 km, which is very close to the global estimate of T_l (72 km) obtained by *Grayver et al.* [2016].

In addition, we estimated oceanic lithosphere thickness beneath the considered islands using the lithosphere age consideration. There is a common consensus that the oceanic lithosphere thickens with age. This thickening occurs by conductive cooling, which converts hot asthenosphere into the lithospheric mantle and causes the oceanic lithosphere to become increasingly thick and dense with age [*Turcotte and Schubert*, 2002; *Lu et al.*,

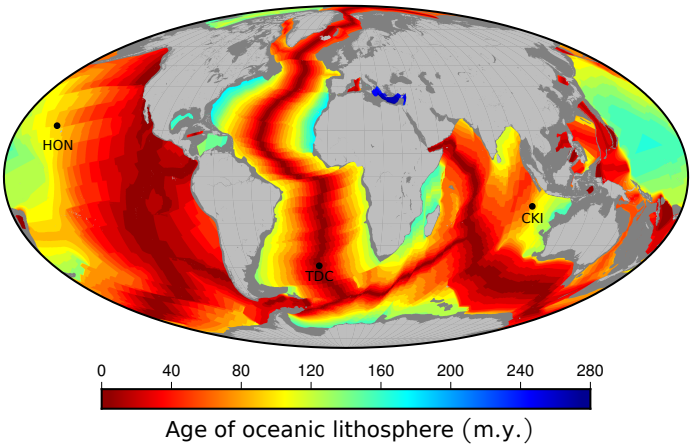

Figure 7. Global distribution of the oceanic lithosphere age. Data is taken from *Müller et al.* [2008].

2021]. Specifically, the age of the lithosphere can be converted into the thickness of the oceanic lithosphere utilizing the following formula [*Ranalli*, 1995]

$$T_l(\theta,\phi) = 2.32\sqrt{\kappa\, a(\theta,\phi)}, \tag{8}$$

where κ is the an average thermal diffusivity for the silicate rocks – taken as $10^{-6}m^2s^{-1}$, cf. Table 7.4 of *Ranalli* [1995] – and a is the laterally-variable age of the lithosphere (cf. Figure 7). We provide in the table the estimates of T_l based on eq. (8) taking lithosphere ages beneath TDC, HON and CKI observatories as 20, 95 and 60 million years [*Müller et al.*, 2008], respectively. As is seen from the table, our estimates of T_l based on a joint inversion of EM TFs generally agree with estimates based on eq. (8), thus confirming a progressive thickening of oceanic lithosphere with age. It is interesting to notice that – in spite of general agreement – our estimates of T_l are systematically ~ 20 km lower than estimates based on eq. (8).

4 Conclusions

We developed a tool to simultaneously invert island multi-source transfer functions in terms of 1-D conductivity distribution. Specifically, we jointly invert magnetotelluric tippers (periods from a few minutes to three hours), new global-to-local (G2L) magnetic transfer functions (periods from a few hours to one day), and global Q-responses (periods from a few days to a few months). Inverting TFs in a broad period range allows us to constrain the conductivity in a wide depth range – from crust to lower mantle. The

critical feature of the tool is a rigorous and accurate account for the ocean induction effect (OIE) which makes the forward problem fully 3-D. OIE is modelled using a nested integral equation approach and invoking high-resolution bathymetry. The inverse problem is solved employing a stochastic algorithm which finds a global minimum and does this for a moderate number of iterations.

We implemented the developed methodology to invert TFs estimated at three islands of different tectonic environments. Beneath two of them – Tristan da Cunha (South Atlantic) and Oahu (North Pacific) – we observe an apparent feature in the recovered profiles – an enhanced conductivity zone, which is in agreement with seismic results suggesting mantle plumes beneath these islands. Besides, the recovered 1-D conductivity profiles indicate oceanic lithosphere of different thicknesses beneath each island, confirming a progressive thickening of oceanic lithosphere with age.

The ongoing work is an implementation of the tool to constrain 1-D conductivity distributions beneath many other islands around the world where long-term magnetic measurements have been performing [*Rigaud et al.*, 2021]. We notice that the tool is designed so that it can be easily adapted to include alternative TFs, like impedances and G2L electric TFs, provided long-period electric field data at islands are also available. Noteworthy, using "electric" TFs allows the probing of high-resistive structures in the lithosphere. Moreover, substituting tippers with impedances enables us to apply the multi-source TFs inversion concept to constrain 1-D conductivity distributions (from crust to lower mantle) beneath *inland* geomagnetic observatories. Such inversion is also a topic of future research, which in particular will include a proper treatment [cf. *Püthe et al.*, 2014] of potential galvanic effects in electric TFs. Finally, we would like to mention that along with TFs originating from the signals of external (either ionospheric or magnetospheric) origin, one can think about adding tidal EM signals (at locations where these signals are reliably detectable) into a joint inversion to further reduce the uncertainties in the recovered 1-D conductivity profiles.

CRediT authorship contribution statement

Chaojian Chen: Methodology, Software, Validation, Formal Analysis, Writing – original draft. **Alexey Kuvshinov**: Conceptualization, Methodology, Formal Anal-

ysis, Funding acquisition, Writing – review & editing. **Mikhail Kruglyakov**: Methodology, Software. **Rafael Rigaud**: Software, Formal Analysis.

Acknowledgments

The authors acknowledge INTERMAGNET (www.intermagnet.org) for promoting the high standards of magnetic observatory practice. We thank the GEBCO Compilation Group (2019), providing high-resolution bathymetry data (the GEBCO_2019 Grid, www.gebco.net). The generic mapping tools (GMT) from *Wessel et al.* [2019] was adopted in plotting the figure of oceanic lithospheric age. CC was partly supported by a grant from the China Scholarship Council Foundation (201806370223). AK and CC have been partially supported in the framework of Swarm DISC activities, funded by ESA contract no. 4000109587, with support from EO Science for Society. MK was supported by the New Zealand Ministry of Business, Innovation & Employment through Endeavour Fund Research Programme contract UOOX2002. RR was supported by Swiss National Science Foundation (grant 200020L-189177/1) awarded through the DACH program.

References

Baba, K., N. Tada, L. Zhang, P. Liang, H. Shimizu, and H. Utada (2013), Is the electrical conductivity of the northwestern Pacific upper mantle normal?, *Geochemistry, Geophysics, Geosystems*, *14*(12), 4969–4979, doi: 10.1002/2013GC004997.

Baba, K., J. Chen, M. Sommer, H. Utada, W. H. Geissler, W. Jokat, and M. Jegen (2017a), Marine magnetotellurics imaged no distinct plume beneath the tristan da cunha hotspot in the southern atlantic ocean, *Tectonophysics*, *716*, 52–63.

Baba, K., N. Tada, T. Matsuno, P. Liang, R. Li, L. Zhang, H. Shimizu, N. Abe, N. Hirano, M. Ichiki, et al. (2017b), Electrical conductivity of old oceanic mantle in the northwestern pacific i: 1-d profiles suggesting differences in thermal structure not predictable from a plate cooling model, *Earth, Planets and Space*, *69*(1), 1–23.

Bahr, K., and J. H. Filloux (1989), Local sq response functions from EMSLAB data, *Journal of Geophysical Research: Solid Earth*, *94*(B10), 14,195–14,200.

Bahr, K., N. Olsen, and T. J. Shankland (1993), On the combination of the magnetotelluric and the geomagnetic depth sounding method for resolving an electrical

conductivity increase at 400 km depth, *Geophysical Research Letters*, *20*(24), 2937–2940.

Banks, R. (1969), Geomagnetic variations and the electrical conductivity of the upper mantle, *Geophysical Journal International*, *17*(5), 457–487.

Becker, J., D. Sandwell, W. Smith, J. Braud, B. Binder, J. Depner, D. Fabre, J. Factor, S. Ingalls, S. Kim, et al. (2009), Global bathymetry and elevation data at 30 arc seconds resolution: Srtm30_plus, *Marine Geodesy*, *32*(4), 355–371.

Berdichevsky, M. N., and V. I. Dmitriev (2008), *Models and methods of magnetotellurics*, Springer Science & Business Media.

Chen, C., M. Kruglyakov, and A. Kuvshinov (2020), A new method for accurate and efficient modeling of the local ocean induction effects. Application to long-period responses from island geomagnetic observatories, *Geophysical Research Letters*, *47*(8), e2019GL086,351.

Chen, C., M. Kruglyakov, and A. Kuvshinov (2021), Advanced three-dimensional electromagnetic modelling using a nested integral equation approach, *Geophysical Journal International*, *226*(1), 114–130.

Egbert, G. D., and J. R. Booker (1992), Very long period magnetotellurics at Tucson observatory: implications for mantle conductivity, *Journal of Geophysical Research: Solid Earth*, *97*(B11), 15,099–15,112.

Fainberg, E., A. Kuvshinov, and B. Singer (1990), Electromagnetic induction in a spherical Earth with non-uniform oceans and continents in electric contact with the underlying medium, II. Bimodal global geomagnetic sounding of the lithosphere, *Geophys. J. Int.*, *102*, 283–286.

Finlay, C., V. Lesur, E. Thébault, F. Vervelidou, A. Morschhauser, and R. Shore (2017), Challenges handling magnetospheric and ionospheric signals in internal geomagnetic field modelling, *Space Science Reviews*, *206*(1), 157–189.

Grayver, A. V., and A. V. Kuvshinov (2016), Exploring equivalence domain in nonlinear inverse problems using Covariance Matrix Adaption Evolution Strategy (CMAES) and random sampling, *Geophysical Journal International*, *205*(2), 971–987.

Grayver, A. V., N. R. Schnepf, A. V. Kuvshinov, T. J. Sabaka, C. Manoj, and N. Olsen (2016), Satellite tidal magnetic signals constrain oceanic lithosphere-asthenosphere boundary, *Science advances*, *2*(9), e1600,798.

Grayver, A. V., F. D. Munch, A. V. Kuvshinov, A. Khan, T. J. Sabaka, and L. Tøffner-Clausen (2017), Joint inversion of satellite-detected tidal and magnetospheric signals constrains electrical conductivity and water content of the upper mantle and transition zone, *Geophysical Research Letters*, *44*(12), 6074–6081.

Guzavina, M., A. Grayver, and A. Kuvshinov (2018), Do ocean tidal signals influence recovery of solar quiet variations?, *Earth, Planets and Space*, *70*, doi: 10.1186/s40623-017-0769-1.

Guzavina, M., A. Grayver, and A. Kuvshinov (2019), Probing upper mantle electrical conductivity with daily magnetic variations using global-to-local transfer functions, *Geophysical Journal International*, *219*(3), 2125–2147.

Hansen, N., and A. Ostermeier (2001), Completely derandomized self-adaptation in evolution strategies, *Evolutionary computation*, *9*(2), 159–195.

Hansen, P. C. (1992), Analysis of discrete ill-posed problems by means of the L-curve, *SIAM review*, *34*(4), 561–580.

Karato, S.-i. (2011), Water distribution across the mantle transition zone and its implications for global material circulation, *Earth and Planetary Science Letters*, *301*(3-4), 413–423.

Key, K. (2016), MARE2DEM: a 2-D inversion code for controlled-source electromagnetic and magnetotelluric data, *Geophysical Journal International*, *207*(1), 571–588.

Key, K., S. Constable, L. Liu, and A. Pommier (2013), Electrical image of passive mantle upwelling beneath the northern East Pacific Rise, *Nature*, *495*, 499–502.

Khan, A. (2016), On Earth's mantle constitution and structure from joint analysis of geophysical and laboratory-based data: An example, *Surveys in Geophysics*, *37*(1), 149–189.

Khan, A., A. Kuvshinov, and A. Semenov (2011), On the heterogeneous electrical conductivity structure of the Earth's mantle with implications for transition zone water content, *J. Geophys. Res.*, *116*, doi:10.1029/2010JB007,458.

Kruglyakov, M., and A. Kuvshinov (2018), Using high-order polynomial basis in 3-D EM forward modeling based on volume integral equation method, *Geophys. J. Int.*, *213*, 1387–1401.

Kuvshinov, A. (2008), 3-D global induction in the oceans and solid Earth: Recent progress in modeling magnetic and electric fields from sources of magnetospheric,

ionospheric and oceanic origin, *Surv. Geophys.*, *29*, doi:10.1007/s10,712–008–9045–z.

Kuvshinov, A., A. Grayver, L. Tøffner-Clausen, and N. Olsen (2021), Probing 3-D electrical conductivity of the mantle using 6 years of Swarm, CryoSat-2 and observatory magnetic data and exploiting matrix Q-responses approach, *Earth, Planets and Space*, *73*(1), 1–26.

Kuvshinov, A. V., N. Olsen, D. B. Avdeev, and O. V. Pankratov (2002), Electromagnetic induction in the oceans and the anomalous behaviour of coastal C-responses for periods up to 20 days, *Geophysical Research Letters*, *29*(12), 36–1.

Larsen, J. (1975), Low frequency (0.1-6.0 cpd) electromagnetic study of deep mantle electrical conductivity beneath the Hawaiian islands, *Geophys. J. R. astr. Soc.*, *43*, 17–46.

Lu, Z., P. Audet, C.-F. Li, S. Zhu, and Z. Wu (2021), What controls effective elastic thickness of the lithosphere in the pacific ocean?, *Journal of Geophysical Research: Solid Earth*, *126*(3), e2020JB021,074.

McAdoo, D. C., and D. T. Sandwell (1985), Folding of oceanic lithosphere, *Journal of Geophysical Research: Solid Earth*, *90*(B10), 8563–8569.

Morschhauser, A., A. Grayver, A. Kuvshinov, F. Samrock, and J. Matzka (2019), Tippers at island geomagnetic observatories constrain electrical conductivity of oceanic lithosphere and upper mantle, *Earth, Planets and Space*, *71*(1), 1–9, doi:10.1186/s40623-019-0991-0.

Müller, R. D., M. Sdrolias, C. Gaina, and W. R. Roest (2008), Age, spreading rates, and spreading asymmetry of the world's ocean crust, *Geochemistry, Geophysics, Geosystems*, *9*(4).

Munch, F. D., A. V. Grayver, A. Kuvshinov, and A. Khan (2018), Stochastic inversion of geomagnetic observatory data including rigorous treatment of the ocean induction effect with implications for transition zone water content and thermal structure, *Journal of Geophysical Research: Solid Earth*, *123*(1), 31–51.

Munch, F. D., A. V. Grayver, M. Guzavina, A. V. Kuvshinov, and A. Khan (2020), Joint inversion of daily and long-period geomagnetic transfer functions reveals lateral variations in mantle water content, *Geophysical Research Letters*, *47*(10), e2020GL087,222.

529 Naif, S., K. Key, S. Constable, and R. Evans (2013), Melt-rich channel observed at
530 the lithosphere-astenosphere boundary, *Nature*, *495*, 356–359.

531 Olsen, N. (1998), The electrical conductivity of the mantle beneath Europe derived
532 from C-responses from 3 to 720 hr, *Geophys. J. Int.*, *133*, 298–308.

533 Parkinson, W., and F. Jones (1979), The geomagnetic coast effect, *Reviews of Geo-*
534 *physics*, *17*(8), 1999–2015.

535 Püthe, C., A. Kuvshinov, and N. Olsen (2014), Handling complex source structures
536 in global EM induction studies: From C-responses to new arrays of transfer func-
537 tions, *Geophys. J. Int.*, doi:10.1093/gji/ggu027.

538 Püthe, C., C. Manoj, and A. Kuvshinov (2014), Reproducing electric field observa-
539 tions during magnetic storms by means of rigorous 3-d modelling and distortion
540 matrix co-estimation, *Earth, Planets and Space*, *66*(1), 1–10.

541 Püthe, C., A. Kuvshinov, and N. Olsen (2015), Handling complex source structures
542 in global EM induction studies: from C-responses to new arrays of transfer func-
543 tions, *Geophysical Journal International*, *201*(1), 318–328.

544 Ranalli, G. (1995), *Rheology of the Earth*, Springer Science & Business Media.

545 Rigaud, R., M. Kruglyakov, A. Kuvshinov, K. Pinheiro, J. Petereit, J. Matzka, and
546 E. Marshalko (2021), Exploring effects in tippers at island geomagnetic observato-
547 ries due to realistic depth- and time-varying oceanic electrical conductivity, *Earth,*
548 *Planets and Space*, *73*(3), doi:10.1186/s40623-020-01339-3.

549 Rychert, C., G. Laske, N. Harmon, and P. Shearer (2013), Seismic imaging of melt
550 in a displaced Hawaiian plume, *Science*, *6*, doi:10.1038/NGEO1878.

551 Rychert, C. A., and P. M. Shearer (2009), A global view of the lithosphere-
552 asthenosphere boundary, *Science*, *324*(5926), 495–498.

553 Rychert, C. A., and P. M. Shearer (2011), Imaging the lithosphere-asthenosphere
554 boundary beneath the pacific using ss waveform modeling, *Journal of Geophysical*
555 *Research: Solid Earth*, *116*(B7).

556 Samrock, F., and A. Kuvshinov (2013), Tippers at island observatories: Can we
557 use them to probe electrical conductivity of the earth's crust and upper mantle?,
558 *Geophysical Research Letters*, *40*(5), 824–828.

559 Schlömer, A., W. Geissler, W. Jokat, and M. Jegen (2017), Hunting for the Tristan
560 mantle plume – An upper mantle tomography around the volcanic island of Tris-
561 tan da Cunha, *Earth and Planet. Sci. Lett.*, *462*, doi:10.1016/j.epsl.2016.12.028.

Schmucker, U. (1970), *Anomalies of geomagnetic variations in the south-western United States*, vol. 13, Bull. Scripps Inst. Ocean, Univ. Calif.

Schmucker, U. (1999a), A spherical harmonic analysis of solar daily variations in the years 1964-1965: response estimates and source fields for global induction-II.Results., *Geophys. J. Int.*, *136*, 455–476.

Schmucker, U. (1999b), A spherical harmonic analysis of solar daily variations in the years 1964-65 – I. Methods, *Geophys. J. Int.*, *136*, 439–454.

Simpson, F., E. Steveling, and M. Leven (2000), The effect of the Hawaiian plume on the magnetic daily variation, *Geophysical Research Letters*, *27*(12), 1775–1778.

Suetsugu, D., H. Shiobara, H. Sugioka, A. Ito, T. Isse, T. Kasaya, N. Tada, K. Baba, N. Abe, and Y. Hamano (2012), TIARES Project: Tomographic investigation by seafloor array experiment for the Society hotspot, *Earth, Planets and Space*, *64(4)*.

Turcotte, D. L., and G. Schubert (2002), *Geodynamics*, Cambridge university press.

Wessel, P., J. Luis, L. Uieda, R. Scharroo, F. Wobbe, W. Smith, and D. Tian (2019), The generic mapping tools version 6, *Geochemistry, Geophysics, Geosystems*, *20*(11), 5556–5564.

Winterbourne, J., A. Crosby, and N. White (2009), Depth, age and dynamic topography of oceanic lithosphere beneath heavily sedimented atlantic margins, *Earth and Planetary Science Letters*, *287*(1-2), 137–151.

Wolfe, C., S. Solomon, G. Laske, J. Collins, R. Detrick, J. Orcutt, D. Bercovici, and E. Hauri (2009), Mantle shear-wave velocity structure beneath the Hawaiian hot spot, *Science*, *326*, doi:10.1126/science.1180165.

Woods, M. T., and E. A. Okal (1996), Rayleigh-wave dispersion along the hawaiian swell: a test of lithospheric thinning by thermal rejuvenation at a hotspot, *Geophysical Journal International*, *125*(2), 325–339.

Woods, M. T., J.-J. Lévêque, E. A. Okal, and M. Cara (1991), Two-station measurements of rayleigh wave group velocity along the hawai'ian swell, *Geophysical Research Letters*, *18*(1), 105–108.

Yamazaki, Y., K. Häusler, and J. A. Wild (2016), Day-to-day variability of midlatitude ionospheric currents due to magnetospheric and lower atmospheric forcing, *Journal of Geophysical Research: Space Physics*, *121*(7), 7067–7086.

Yoshino, T., and T. Katsura (2013), Electrical conductivity of mantle minerals: role of water in conductivity anomalies, *Annual review of earth and planetary sciences*, *41*, 605–628.